Thermal Stress Prediction in Laser Powder Bed Fusion

Tao Liu[1], Edward C. Kinzel[2], Ming C. Leu[1]
[1]Mechanical and Aerospace Engineering Department, Missouri University of Science and Technology, Rolla, MO 65409, USA
[2]Aerospace and Mechanical Engineering Department, University of Notre Dame, Notre Dame, IN 46556, USA

Abstract

This research applies Green's function solutions to simulate temperature and thermal stress fields in laser powder-bed fusion (LPBF) processes. Using a semi-infinite domain and 2D Gaussian laser profiles, the analytical model achieves high computational efficiency, has the potential for real-time controls and predictions in LPBF processes. The model highlights the role of principal stresses in determining crack formations, aligning closely with experimental results.

1. Introduction

The laser powder-bed fusion (LPBF) process stands as a pivotal technique in additive manufacturing, known for its proficiency in crafting products with high dimensional accuracy and complex geometries [1]. A crucial element in this domain is fast multiscale-multiphysics modeling [2] which facilitates the model-driven feedforward control of the temperature field [3], inherent strain homogenization [4], and deformation prediction[5], thereby enhancing the manufacturing process. Furthermore, these models can be seamlessly integrated with in-situ monitoring systems [6,7] to bolster the prediction of defects[8], porosity [9], and powder properties [10,11], steering towards the real-time digital twin of additive manufacturing [12,13].

Despite considerable advancements in computational modeling of multiphysics at various scales, the dominant focus has remained on finite difference [14,15] or finite element methods [16,17]. These approaches suffer from low computational efficiency hindering their real-time implementation. Analytical solutions emerge as a viable alternative, offering higher computational efficiency compared to numerical models [18] and enabling an explicit representation of correlations between material properties, scanning strategies, laser power parameters, and the end performance of the produced part [19].

A promising avenue in this area is the application of Green's function for simulating temperature and thermal stress fields, which significantly enhances computational speed and efficiency [19,20,21]. The inherent parallel computing capabilities of Green's functions align well with the requirements of high-performance computing environments, offering compatibility with cloud-based computer clusters [22].

In this paper, the temperature field originating from a semi-infinite domain heated by a 2D Gaussian profile laser beam is studied. Green's function solution for this temperature field is represented, laying the groundwork to calculate the temperature field history according to arbitrary scanning strategies. Furthermore, the displacement equilibrium equation— also known as the Navier equation — for a semi-infinite domain with a traction-free surface is discussed, denoting the Green's function solution and delineating all components of the final thermal stress tensor. The results are validated through a comparison with experimental results from other researcher's results.

2. Temperature Field of Semi Infinite Domains

The heat transport model under investigation is illustrated in Fig. 1. In this model, the printing laser scans the top surface of a semi-infinite domain. To simulate the laser source utilized in printing, a 2D Gaussian profile is employed, which is represented as:

$$q(x,y)=\frac{2P_0}{\pi R_0^2}e^{-2\frac{(x-x_0)^2+(y-y_0)^2}{R_0^2}} \tag{1}$$

where $(x_0,y_0,0)$ denotes the central coordinate of the heat source, while R_0 refers to the radius of the Gaussian circle. To ensure that the total absorbed heat power meets the condition $P_0(t)$, the coefficients in the expression are chosen as reflected in the equation:

$$\int_{-\infty}^{\infty}\int_{-\infty}^{\infty} q(x,y)\,dxdy=\frac{2P_0}{\pi R_0^2}\int_{-\infty}^{\infty} e^{-2\frac{(x-x_0)^2}{R_0^2}}dx\int_{-\infty}^{\infty} e^{-2\frac{(y-y_0)^2}{R_0^2}}dy=\frac{2P_0}{\pi R_0^2}\sqrt{\frac{\pi R_0^2}{2}}\sqrt{\frac{\pi R_0^2}{2}}=P_0 \tag{2}$$

The heat transport phenomenon in a semi-infinite medium obeys the following equation:

$$\begin{cases}\dfrac{\partial T(x,y,z,t)}{\partial t}-\dfrac{k}{\rho c}\nabla^2 T(x,y,z,t)=\dfrac{q(x,y,t)}{\rho c}\\ B.C.\quad k\dfrac{\partial T(x,y,z,t)}{\partial z}\Big|_{z=0}=0\\ I.C.\qquad T(x,y,z,0)=T_0\end{cases} \tag{3}$$

where the variables k, ρ, c are indicative of the thermal conductivity, density, and specific heat, respectively. The model assumes material properties that are independent of temperature. Initial conditions are defined by a temperature T_0 and an adiabatic surface. The analysis leverages several assumptions: the material is homogeneous and isotropic, elastic deformation does not influence the temperature field, and no phase transformations or precipitations are involved. Additionally, the volumetric heat absorption is neglected in this study.

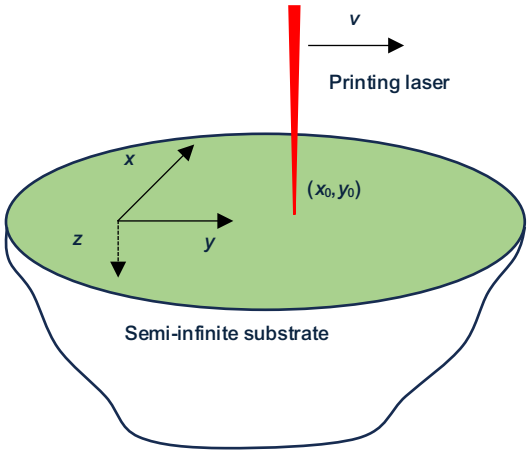

Fig. 1. Illustration of the laser printing process.

The analytical Green's function solution to the heat equation is given by the expression:

$$T(x,\tau)=T_0+\frac{\alpha}{k}\int_0^t d\tau\frac{2P_0(t)}{\pi\left[R_0^2+8\alpha(t-\tau)\right]\sqrt{\pi\alpha(t-\tau)}}e^{-2\frac{(x-x_0)^2+(y-y_0)^2}{R_0^2+8\alpha(t-\tau)}-\frac{z^2}{4\alpha(t-\tau)}} \tag{4}$$

where α denotes thermal diffusivity and is defined as $\alpha = k/\rho c$. Figure 2 presents the fields of temperature during the laser scanning process, delineated by a dashed line with an arrow to indicate a meandering scanning strategy. By applying a predetermined scanning strategy defined by coordinates (x_0, y_0), it becomes possible to quickly obtain the temperature field. Solving the heat equation with a moving laser source through commercial finite element software can be incredibly time-consuming, often requiring hundreds of hours. In contrast, utilizing the analytical solution, the temperature field in Fig. 2 is obtained less than one second.

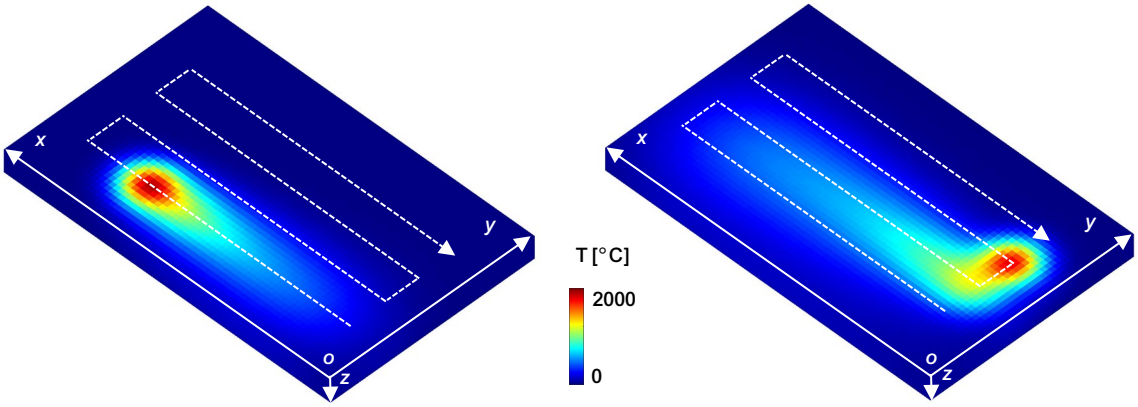

Fig. 2. Temperature field at different scanning time predicted by the analytical solution.

3. Quasi-Static Thermoelasticity

The compatibility condition establishing the relationship between the displacement u and strain ε is expressed as

$$\begin{pmatrix}\varepsilon_{xx} & \varepsilon_{xy} & \varepsilon_{xz}\\ \varepsilon_{yx} & \varepsilon_{yy} & \varepsilon_{yz}\\ \varepsilon_{zx} & \varepsilon_{zy} & \varepsilon_{zz}\end{pmatrix}=\begin{pmatrix}\frac{\partial u_x}{\partial x} & \frac{1}{2}\left(\frac{\partial u_y}{\partial x}+\frac{\partial u_x}{\partial y}\right) & \frac{1}{2}\left(\frac{\partial u_z}{\partial x}+\frac{\partial u_x}{\partial z}\right)\\ \frac{1}{2}\left(\frac{\partial u_x}{\partial y}+\frac{\partial u_y}{\partial x}\right) & \frac{\partial u_y}{\partial y} & \frac{1}{2}\left(\frac{\partial u_z}{\partial y}+\frac{\partial u_y}{\partial z}\right)\\ \frac{1}{2}\left(\frac{\partial u_x}{\partial z}+\frac{\partial u_z}{\partial x}\right) & \frac{1}{2}\left(\frac{\partial u_y}{\partial z}+\frac{\partial u_z}{\partial y}\right) & \frac{\partial u_z}{\partial y}\end{pmatrix} \tag{5}$$

Within the material's interior point, the displacement vector u comprises three components, whereas the strain tensor ε has nine components. The isotropic material's Hook's Law, accounting for thermal expansion, is represented by:

$$\begin{pmatrix}\sigma_{xx} & \sigma_{xy} & \sigma_{xz}\\ \sigma_{yx} & \sigma_{yy} & \sigma_{yz}\\ \sigma_{zx} & \sigma_{zy} & \sigma_{zz}\end{pmatrix}=2\mu\begin{pmatrix}\varepsilon_{xx} & \varepsilon_{xy} & \varepsilon_{xz}\\ \varepsilon_{yx} & \varepsilon_{yy} & \varepsilon_{yz}\\ \varepsilon_{zx} & \varepsilon_{zy} & \varepsilon_{zz}\end{pmatrix}+\left[\lambda\varepsilon_{kk}-\gamma\left(T-T_0\right)\right]\begin{pmatrix}1 & 0 & 0\\ 0 & 1 & 0\\ 0 & 0 & 1\end{pmatrix} \tag{6}$$

In this equation, γ is determined by $\alpha_L(3\lambda + 2\mu)$, where α_L, λ, μ are the thermal expansion, lame parameter and shear modulus, respectively. T is the temperature from Eq. (4). The

summation of the normal stresses, ε_{kk}, is denoted by $\varepsilon_{kk} = \varepsilon_{xx} + \varepsilon_{yy} + \varepsilon_{zz}$. Here, σ stands for the stress tensor encompassing nine components. The equation of motion is depicted as:

$$\begin{aligned}
&\frac{\partial \sigma_{xx}}{\partial x} + \frac{\partial \sigma_{xy}}{\partial y} + \frac{\partial \sigma_{xz}}{\partial z} + X_x = \rho \frac{\partial^2 u_x}{\partial t^2} \\
&\frac{\partial \sigma_{yx}}{\partial x} + \frac{\partial \sigma_{yy}}{\partial y} + \frac{\partial \sigma_{yz}}{\partial z} + X_y = \rho \frac{\partial^2 u_y}{\partial t^2} \\
&\frac{\partial \sigma_{zx}}{\partial x} + \frac{\partial \sigma_{zy}}{\partial y} + \frac{\partial \sigma_{zz}}{\partial z} + X_z = \rho \frac{\partial^2 u_z}{\partial t^2}
\end{aligned} \tag{7}$$

where X is the body force vector and the terms on the equation's right side represents acceleration. Given that the body force X, primarily gravity, is substantially lesser than the stress divergence, it is disregarded in this analysis. Assuming a quasi-static scenario nullifies the acceleration term as well. Substituting the compatibility condition (Eq. (5)) and Hook's law (Eq. (6)) into the equation of motion (Eq. (7)), derives the following displacement equilibrium equation (Navier equation):

$$\begin{cases}
\mu\left(\frac{\partial^2 u_x}{\partial x^2} + \frac{\partial^2 u_x}{\partial y^2} + \frac{\partial^2 u_x}{\partial z^2}\right) + (\mu+\lambda)\frac{\partial}{\partial x}\left(\frac{\partial u_x}{\partial x} + \frac{\partial u_y}{\partial y} + \frac{\partial u_z}{\partial z}\right) - \gamma\frac{\partial T}{\partial x} = 0 \\
\mu\left(\frac{\partial^2 u_y}{\partial x^2} + \frac{\partial^2 u_y}{\partial y^2} + \frac{\partial^2 u_y}{\partial z^2}\right) + (\mu+\lambda)\frac{\partial}{\partial y}\left(\frac{\partial u_x}{\partial x} + \frac{\partial u_y}{\partial y} + \frac{\partial u_z}{\partial z}\right) - \gamma\frac{\partial T}{\partial y} = 0 \\
\mu\left(\frac{\partial^2 u_z}{\partial x^2} + \frac{\partial^2 u_z}{\partial y^2} + \frac{\partial^2 u_z}{\partial z^2}\right) + (\mu+\lambda)\frac{\partial}{\partial z}\left(\frac{\partial u_x}{\partial x} + \frac{\partial u_y}{\partial y} + \frac{\partial u_z}{\partial z}\right) - \gamma\frac{\partial T}{\partial z} = 0
\end{cases} \tag{8}$$

The Lame parameter (λ) and shear modulus (μ) can be expressed in terms of Young's modulus (E) and Poisson's ratio (v) as shown:

$$\begin{aligned}
\lambda &= \frac{Ev}{(1+v)(1-2v)} \\
\mu &= \frac{E}{2(1+v)}
\end{aligned} \tag{9}$$

Setting the boundary conditions for the Navier equation involves defining a traction-free surface as:

$$\sigma_{zz} = \sigma_{zx} = \sigma_{zy} = 0 \tag{10}$$

The displacement solution u to the Navier equation Eq. (8), at the point (ξ_x, ξ_y, ξ_z), is formulated as:

$$\begin{cases}
u_x(\xi_x,\xi_y,\xi_z) = \gamma\int_V (T(x,y,z) - T_0) U_{k,k}^{(x)}(x,y,z \mid \xi_x,\xi_y,\xi_z)\, dxdydz \\
u_y(\xi_x,\xi_y,\xi_z) = \gamma\int_V (T(x,y,z) - T_0) U_{k,k}^{(y)}(x,y,z \mid \xi_x,\xi_y,\xi_z)\, dxdydz \\
u_z(\xi_x,\xi_y,\xi_z) = \gamma\int_V (T(x,y,z) - T_0) U_{k,k}^{(z)}(x,y,z \mid \xi_x,\xi_y,\xi_z)\, dxdydz
\end{cases} \tag{11}$$

where the dilatation term $U^{(n)}_{k,k}(x, y, z|\xi_x, \xi_y, \xi_z)$ is the divergence of the displacement u instigated by a unite force $\delta(x - \xi_x, y - \xi_y, z - \xi_z)$ at the point (ξ_x, ξ_y, ξ_z) along x_n direction. It can be outlined as

$$U_{k,k}^{(x)}=\frac{-1}{4\pi\left(2\mu+\lambda\right)}\left[\frac{x-\xi_x}{R^3}+\frac{\lambda+3\mu}{\lambda+\mu}\frac{x-\xi_x}{R_1^{\,3}}+2z'\frac{3\left(\xi_x-x\right)\left(z+\xi_z\right)}{R_1^{\,5}}\right]$$

$$U_{k,k}^{(y)}=\frac{-1}{4\pi\left(2\mu+\lambda\right)}\left[\frac{y-\xi_y}{R^3}+\frac{\lambda+3\mu}{\lambda+\mu}\frac{y-\xi_y}{R_1^{\,3}}+2z'\frac{3\left(\xi_y-y\right)\left(z+\xi_z\right)}{R_1^{\,5}}\right] \tag{12}$$

$$U_{k,k}^{(z)}=\frac{-1}{4\pi\left(2\mu+\lambda\right)}\left[\frac{z-\xi_z}{R^3}+\frac{\lambda+3\mu}{\lambda+\mu}\frac{z+\xi_z}{R_1^{\,3}}+2z'\frac{2\left(z+\xi_z\right)^2-\left(\xi_y-y\right)^2-\left(\xi_x-x\right)^2}{R_1^{\,5}}\right]$$

where the R is the distance between (x, y, z) and (ξ_x, ξ_y, ξ_z) and R_1 is the distance between $(x, y, -z)$ and (ξ_x, ξ_y, ξ_z) calculated as

$$\begin{aligned}R&=\left(\xi_x-x\right)^2+\left(\xi_y-y\right)^2+\left(\xi_z-z\right)^2\\ R_1&=\left(\xi_x-x\right)^2+\left(\xi_y-y\right)^2+\left(\xi_z+z\right)^2\end{aligned} \tag{13}$$

The final thermal stress can be determined by substituting the calculated displacement from Eq. (11) into the compatibility condition Eq. (5) and Hook's law Eq. (6), yielding:

$$\begin{aligned}\sigma_{xx}&=2\mu\frac{\partial u_x}{\partial x}+\lambda\left(\frac{\partial u_x}{\partial x}+\frac{\partial u_y}{\partial y}+\frac{\partial u_z}{\partial z}\right)-\gamma\left(T-T_0\right)\\ \sigma_{xy}&=\mu\left(\frac{\partial u_x}{\partial y}+\frac{\partial u_y}{\partial x}\right)\\ \sigma_{xz}&=\mu\left(\frac{\partial u_x}{\partial z}+\frac{\partial u_z}{\partial x}\right)\\ \sigma_{yx}&=\mu\left(\frac{\partial u_y}{\partial x}+\frac{\partial u_x}{\partial y}\right)\\ \sigma_{yy}&=2\mu u_{y,y}+\lambda\left(\frac{\partial u_x}{\partial x}+\frac{\partial u_y}{\partial y}+\frac{\partial u_z}{\partial z}\right)-\gamma\left(T-T_0\right)\\ \sigma_{yz}&=\mu\left(\frac{\partial u_y}{\partial z}+\frac{\partial u_z}{\partial y}\right)\\ \sigma_{zx}&=\mu\left(\frac{\partial u_z}{\partial x}+\frac{\partial u_x}{\partial z}\right)\\ \sigma_{zy}&=\mu\left(\frac{\partial u_z}{\partial y}+\frac{\partial u_y}{\partial z}\right)\\ \sigma_{zz}&=2\mu\frac{\partial u_z}{\partial z}+\lambda\left(\frac{\partial u_x}{\partial x}+\frac{\partial u_y}{\partial y}+\frac{\partial u_z}{\partial z}\right)-\gamma\left(T-T_0\right)\end{aligned} \tag{14}$$

Figure 3 shows the predicted thermal stress field incorporating all nine components. It reveals that the shear stresses are considerably less than the normal stresses, which proves that these three normal stresses (σ_{xx}, σ_{yy}, σ_{zz}) are almost the principal stresses and the contribution of the shear stresses (σ_{xy}, σ_{xz}, σ_{yx}, σ_{yz}, σ_{zx}, σ_{zy}) can be neglected.

Comparative analysis with experimental data from existing literature can validate these analytical thermal stress predictions. Figure 4 from reference [23], for instance, delineates the morphology of a single-track ternary ceramic under varied process parameters, where σ_{xx} aligns with the scanning direction, and σ_{yy} is orthogonal to it. The figure exhibits transverse cracks induced by thermal stress σ_{xx}, and longitudinal fissures attributable to stress σ_{yy}. A conspicuous absence of 45° cracks corroborates the negligible role of shear stress, aligning seamlessly with the analytical predictions of thermal stress outcomes.

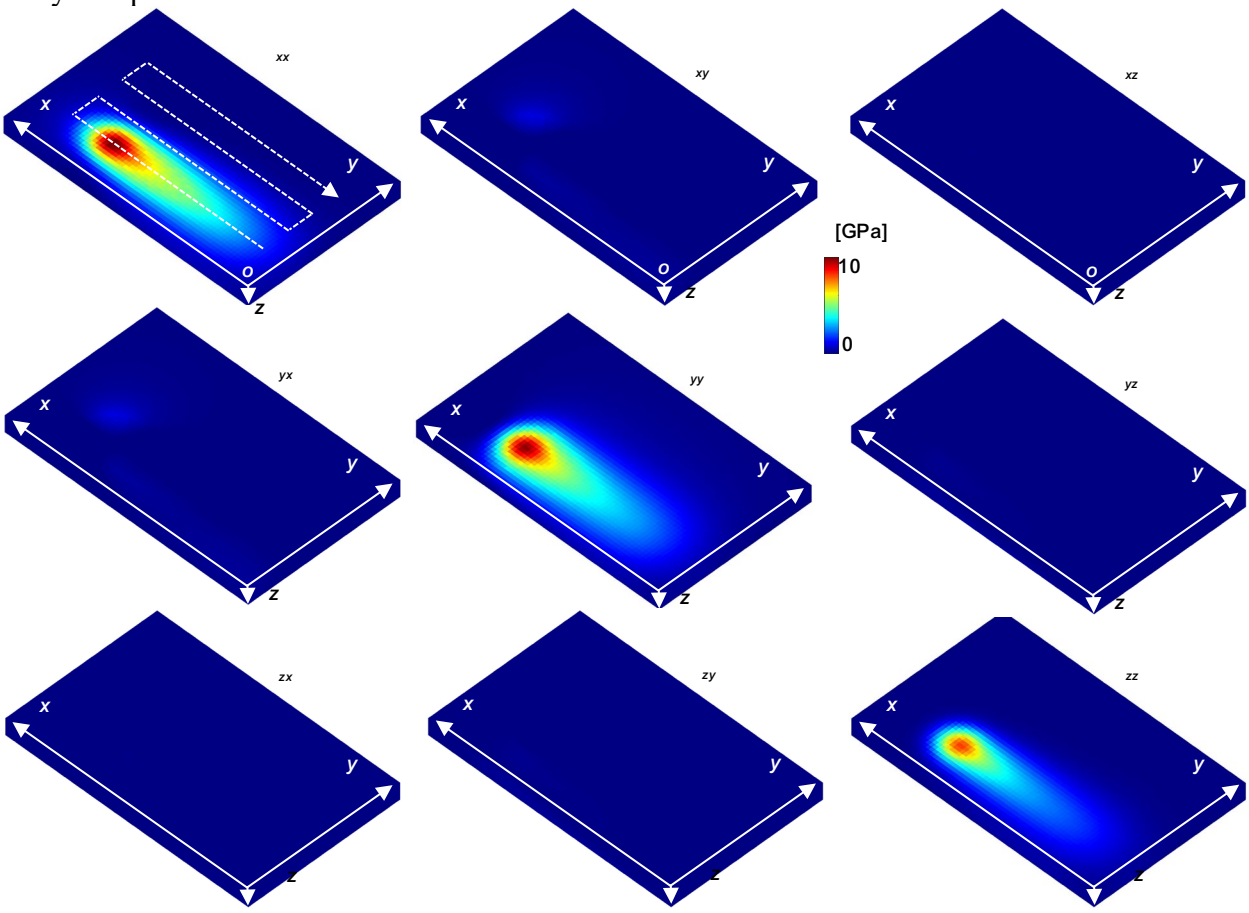

Fig. 3. Thermal stress field predicted by the analytical solution.

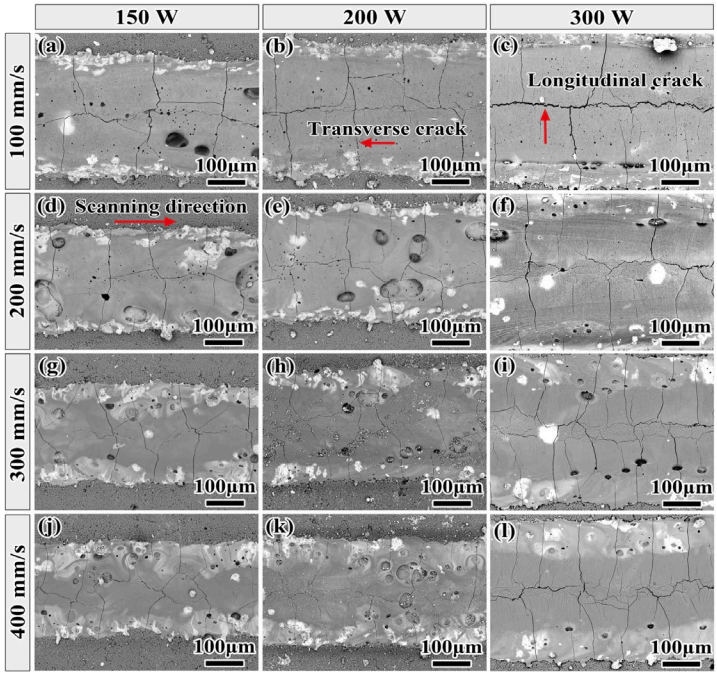

Fig. 4. Morphology of single-track ternary ceramic at different laser process parameters [23].

4. Conclusion

In conclusion, this study rigorously delineated a multiscale-multiphysics modeling approach employing Green's function solutions for simulating the temperature field and thermal stress field in the context of LPBF processes. Through the incorporation of semi-infinite domain analysis and 2D Gaussian profile laser beam, the study unearthed pivotal insights into the dynamics of temperature fields, paving avenues for rapid and precise simulations that are aligned with high-performance computing requisites. Furthermore, the deployment of Navier equations in a semi-infinite domain calculated displacement and stress fields, thereby unraveling the predominant role of principal stresses in the crack formations. These analytical solutions presented herein show better computational efficiency and a potential in real-time control and monitoring of LPBF processes, pave a path towards the realization of a real-time digital twin in additive manufacturing.

Reference

1. R. Yavari, R. Williams, A. Riensche, P.A. Hooper, K.D. Cole, L. Jacquemetton, H. (Scott) Halliday, P.K. Rao, Thermal modeling in metal additive manufacturing using graph theory – Application to laser powder bed fusion of a large volume impeller, Addit Manuf. 41 (2021) 101956.
2. M. Bayat, W. Dong, J. Thorborg, A.C. To, J.H. Hattel, A review of multi-scale and multi-physics simulations of metal additive manufacturing processes with focus on modeling strategies, Addit. Manuf. 47 (2021) 102278.
3. A. Riensche, B.D. Bevans, Z. Smoqi, R. Yavari, A. Krishnan, J. Gilligan, N. Piercy, K. Cole, P. Rao, Feedforward control of thermal history in laser powder bed fusion: Toward physics-based optimization of processing parameters, Mater Design. 224 (2022) 111351.
4. X. Liang, W. Dong, Q. Chen, A.C. To, On incorporating scanning strategy effects into the modified inherent strain modeling framework for laser powder bed fusion, Addit. Manuf. 37 (2021) 101648.
5. W. Dong, X. Liang, Q. Chen, S. Hinnebusch, Z. Zhou, A.C. To, A new procedure for implementing the modified inherent strain method with improved accuracy in predicting both residual stress and deformation for laser powder bed fusion, Addit. Manuf. 47 (2021) 102345.

6. T. Liu, E.C. Kinzel, M.C. Leu, In-Situ Infrared Thermographic Measurement of Powder Properties in Laser Powder Bed, 2022 International Solid Freeform Fabrication Symposium. (2022).
7. T. Liu, C.S. Lough, H. Sehhat, J. Huang, E.C. Kinzel, M.C. Leu, In-Situ Thermographic Inspection for Laser Powder .pdf, 2021 International Solid Freeform Fabrication Symposium. (2021).
8. C.S. Lough, X. Wang, C.C. Smith, R.G. Landers, D.A. Bristow, J.A. Drallmeier, B. Brown, E.C. Kinzel, Correlation of SWIR imaging with LPBF 304L stainless steel part properties, Addit Manuf. 35 (2020) 101359.
9. C.S. Lough, T. Liu, X. Wang, B. Brown, R.G. Landers, D.A. Bristow, J.A. Drallmeier, E.C. Kinzel, Local prediction of Laser Powder Bed Fusion porosity by short-wave infrared imaging thermal feature porosity probability maps, J Mater Process Tech. 302 (2022) 117473.
10. T. Liu, E.C. Kinzel, M.C. Leu, In-Situ Lock-in Thermographic Measurement of Powder Layer Thermal Diffusivity and Thickness in Laser Powder Bed Fusion, Addit. Manuf. (2023) 103726.
11. T. Liu, C.S. Lough, H. Sehhat, Y.M. Ren, P.D. Christofides, E.C. Kinzel, M.C. Leu, In-situ infrared thermographic inspection for local powder layer thickness measurement in laser powder bed fusion, Addit Manuf. 55 (2022) 102873.
12. A. Gaikwad, R. Yavari, M. Montazeri, K. Cole, L. Bian, P. Rao, Toward the digital twin of additive manufacturing: Integrating thermal simulations, sensing, and analytics to detect process faults, Iise Transactions. 52 (2020) 1204–1217.
13. D.R. Gunasegaram, A.B. Murphy, A. Barnard, T. DebRoy, M.J. Matthews, L. Ladani, D. Gu, Towards developing multiscale-multiphysics models and their surrogates for digital twins of metal additive manufacturing, Addit Manuf. 46 (2021) 102089.
14. C. He, K.S. Ramani, C.E. Okwudire, An intelligent scanning strategy (SmartScan) for improved part quality in multi-laser PBF additive manufacturing, Addit. Manuf. 64 (2023) 103427.
15. K.S. Ramani, C. He, Y.-L. Tsai, C.E. Okwudire, SmartScan: An intelligent scanning approach for uniform thermal distribution, reduced residual stresses and deformations in PBF additive manufacturing, Addit Manuf. 52 (2022) 102643.
16. P. Köhnen, S. Ewald, J.H. Schleifenbaum, A. Belyakov, C. Haase, Controlling microstructure and mechanical properties of additively manufactured high-strength steels by tailored solidification, Addit Manuf. 35 (2020) 101389.
17. P. Zagade, B.P. Gautham, A. De, T. DebRoy, Analytical estimation of fusion zone dimensions and cooling rates in part scale laser powder bed fusion, Addit Manuf. 46 (2021) 102222.
18. J.C. Steuben, A.J. Birnbaum, J.G. Michopoulos, A.P. Iliopoulos, Enriched analytical solutions for additive manufacturing modeling and simulation, Addit Manuf. 25 (2019) 437–447.
19. N.A. Apetre, J.G. Michopoulos, J.C. Steuben, A.J. Birnbaum, A.P. Iliopoulos, Analytical thermoelastic solutions for additive manufacturing processes, Addit Manuf. 56 (2022) 102892.
20. T.F. Flint, J.A. Francis, M.C. Smith, A.N. Vasileiou, Semi-analytical solutions for the transient temperature fields induced by a moving heat source in an orthogonal domain, Int J Therm Sci. 123 (2018) 140–150.
21. V. Şeremet, A new approach to constructing Green's functions and integral solutions in thermoelasticity, Acta Mech. 225 (2014) 735–755.
22. A.J. Wolfer, J. Aires, K. Wheeler, J.-P. Delplanque, A. Rubenchik, A. Anderson, S. Khairallah, Fast solution strategy for transient heat conduction for arbitrary scan paths in additive manufacturing, Addit Manuf. 30 (2019) 100898.
23. Z. Shen, H. Su, M. Yu, Y. Guo, Y. Liu, D. Zhao, H. Jiang, P. Yang, M. Yang, Z. Zhang, M. Guo, W. Ren, Large-size complex-structure ternary eutectic ceramic fabricated using laser powder bed fusion assisted with finite element analysis, Addit. Manuf. 72 (2023) 103627.